Low resistivity amorphous carbon-based thin films employed as anti-reflective coatings on copper

Ângela Elisa Crespi, Charles Ballage, Marie Christine Hugon, Jacques Robert, Daniel Lundin, Ian Vickridge, José Alvarez, Tiberiu Minea

Low resistivity amorphous carbon-based thin films employed as anti-reflective coatings on copper

Ângela Elisa Crespi [a, *], Charles Ballage [a], Marie Christine Hugon [a], Jacques Robert [a], Daniel Lundin [a, b], Ian Vickridge [c], José Alvarez [d], Tiberiu Minea [a]

[a] Laboratoire de Physique des Gaz et Plasmas, LPGP, Université Paris-Saclay, CNRS, F-91405 Orsay Cedex, France
[b] Plasma & Coatings Physics Division, IFM, Linköping University, SE-581 83 Linköping, Sweden
[c] Institut de nanosciences de Paris, INSP, Sorbonne Université - Case 840 - 4 place Jussieu Barre 1222, 75005 Paris, France
[d] Génie électrique et électronique de Paris Saclay, GeePS, Université Paris-Saclay, Sorbonne Université, CNRS, Plateau de Moulon 91192 Gif sur Yvette Cedex France

ABSTRACT

Amorphous carbon-based coatings deposited on copper substrates by magnetron sputtering at different target-to-substrate distances were investigated. Films deposited at short distances as 2 cm presented the best results in terms of morphology, density, and resistivity. Ultraviolet near-infrared range spectrometry measurements determined total reflectance and ellipsometry, extinction coefficient, refraction index, and pseudo bandgap. Amorphous carbon films of 150 nm deposited at 2 cm reduced the total reflectance by up to 60 ± 5% in the near-infra-red range when compared to pure copper films. The addition of Fe*boosts the absorption of the coating reducing the total reflectance by up to 70 ± 5% in near-infrared. (Fe*: deposited from stainless-steel target used in direct-current magnetron sputtering). Also, it reduces the electrical resistivity by a factor of 100 compared to that of pure amorphous carbon films. The reduction in total reflectance induced by the presence of the amorphous carbon-based films on copper depends, as expected, on light penetration depth and the absorption coefficient.

1. Introduction

The know-how to reduce or eliminate reflection over a broadband spectrum is of great importance for several applications. Examples include artificial blackbodies, photodetectors, stray light shields, infrared imaging, stealth technology, and solar energy absorption [1,2]. In recent years several promising approaches have emerged. Laser irradiation has been used to darken metals as a strategy to drastically reduce reflection [3–6]. Anti-reflective coatings on copper using an ultra-rapid pulsed laser produces periodic microstructure arrays on the surface for light trapping [2]. These processes dramatically reduced the specular reflection by blackening the copper surface, resulting in reflectivity of about 6% in the visible spectrum, comparing to almost 100% for pure copper [2,7].

Despite the tremendous progress of anti-reflective coatings of well-aligned one-dimensional nanostructures, such as carbon nanotubes, or 2D velvet-like carbon [8], a much simpler solution using amorphous carbon films (a-C) has also been shown to reduce reflection from the near UV to IR broadband spectrum [9–11]. Such a solution has the advantage that it is straightforward to implement in industrial thin film deposition [12–14].

The electrical and optical properties of a-C films are connected. The study of Chhowalla et al. [15] showed that the optical and electrical properties depend on the fraction of sp^2 carbon in the material. Indeed, the conduction band joins the valence band locally due to the sp^2 orbitals - the so-called pseudo-band gap. The size of the pseudo-band gap is indicative of the electrical properties of the amorphous C, depending on the mixture sp^2-sp^3 in the films [9,15,16]. The optical properties of the amorphous carbon (a-C) are directly related to $\pi \rightarrow \pi^*$ and $\sigma \rightarrow \sigma^*$ electronic transitions, which determine the characteristic colour of the film, ranging from transparent if very few electronic transitions occur in the material to dark where many electronic transitions are simultaneously possible in the film. Generally, high resistivity carbon materials (sp^3 dominant) are more transparent than the conductive ones, such as sputtered a-C (sp^2 dominant) or graphite-like carbon [17,18].

Even though a-C films composed principally of sp2 states generally exhibit lower resistivity, electrical conductivity may vary by up to 12 orders of magnitude depending on the ratio and distribution of the sp2 to sp3 bonds. Furthermore, the addition of metal into the amorphous carbon matrix a-C:Me (0–100% at) enhances its conductivity [19,20]. A metal atom, such as Fe, Ni, Cr can either bound to form a carbide or it can disperse into the carbon matrix due to the relatively high mobility of the metallic *adatoms* [20,21]. In both cases, they create conductive paths, when the concentration of the metal is high enough to establish contact between the metallic particles, referred to as the *percolation threshold* [21]. These metals are largely used to catalyse the sp^2 structure of carbon leading, for instance to nanotubes or nanofibers [22]. Also, the optical bandgap of amorphous metal-rich films decreases continuously with increasing metal content with the precise evolution depending on the specific metal, resulting in better light absorption [20,23,24]. If the doping element is sufficiently energetic and mobile, it will find a location that adds new energy states in the open gap (by filling dangling bonds) reducing the resistivity of the film [25,26].

In the case of iron-doped amorphous carbon films (a-C:Fe) (2% at.), the resistivity is one order of magnitude lower than that measured for the same film of pure a-C [27]. Concerning the *percolation threshold*, it was found for polymers doped with iron nanoparticles to be 12% at. of Fe [28]. The choice of using Fe from a stainless-steel (SS) target, noted Fe* hereafter, is motivated by its cost and the enhancement of optical constants of the deposited carbon-based films. Craic et al. [29] reported several improvements on a-C:H/stainless-steel/Cu multilayers, the metal-rich component layer absorbs light and, the metal-free a-C:H acts as a front surface anti-reflection layer [30].

Although carbon-based thin films have been extensively studied, the use of these thin films as a strategy to dye or darken very reflective surfaces, such as silver or copper, is still in its early stages. The objective of this work is to explore the optical and electrical properties of thin a-C and a-C:Fe* films deposited by direct current magnetron sputtering (DCMS) onto Cu substrates. The advantage of the C/Cu layer configuration is that interaction between these two elements only occurs under very specific conditions of temperature and energy [31,32], which opens up for new creative solutions in industrial applications. In the present study, we investigated the film microstructure varying the target-to-substrate distance (TSD); The capacity to absorb light in the broadband ultra-violet-visible (UV–Vis) (400–1000 nm) spectrum as a function of film microstructure and composition; Also, the electrical resistivity of the deposited a-C and a-C:Fe* films.

2. Materials and methods

The carbon thin films were grown onto a thin mirror-like copper coating previously deposited onto Si (100) substrates of around 22.5 mm^2 to 62.5 mm^2 (resistivity $\rho_{Si} = 10–14\ \Omega.cm$) using DCMS. Before film deposition, each Si substrate was ultrasonically cleaned in acetone (30 min) and isopropanol (30 min) and then loaded into the grounded deposition sample holder, playing the role of anode.

The copper films were deposited in a custom-built vacuum chamber evacuated by a turbo-molecular pump to a base pressure below 3×10^{-4} Pa. The deposition system was equipped with a copper target (99.99% purity) 6 in. top-mounted water-cooled magnetron. A load-lock chamber was employed for transferring the samples by using a movable sample-holder facing the target. The target-to-substrate distance was fixed at 13.5 cm for all copper depositions. The copper films were grown using Ar (99.997% purity) as working gas at a total pressure of 0.5 Pa. The thickness of the films was on average 200 ± 20 nm. The DC voltage applied to the magnetron was constant at 300 V. The resistivity of the copper films was around 5 μΩ.cm (Cu bulk 1.67 μΩ.cm), which is in agreement with a previous study [33].

In a second deposition step, carbon thin films were deposited onto the copper films (Fig. 1a)), referred to as a-C/Cu. This step was carried out in a smaller deposition system also evacuated by a turbo-molecular pump to a base pressure below 3×10^{-3} Pa using as working gas Ar (99.997% purity) at a total pressure of 0.75 Pa. A carbon target (99.999% purity) 1 in. was clamped in a top-mounted water-cooled magnetron, also operated in DC mode at fixed power for all carbon-based samples of this work 55 ± 2 W.

For a-C:Fe* films, we employed a mixed stainless-steel/carbon target. A stainless-steel ring, composition AISI 316 (1 in. diameter), was positioned around the edge of the carbon target to produce a mixed sputtering. The final film layer structure, referred to hereafter as a-C:Fe*/Cu, is schematically represented in Fig. 1b). The notation Fe* indicates that films may contain traces of Ni and Cr more than Fe due to the AISI 316 composition. All films were deposited at room temperature (i.e., no additional heating was provided to the substrate). The thickness of the a-C films and a-C:Fe* was varied, although typically maintained at about 150 nm ± 10 nm. The deposition rates for each target-to-substrate distance are summarized in Table 1. In both cases, the deposition rate decreased significantly with increasing TSD (up to 94% and 95% for a-C and a-C:Fe* films, respectively) in the investigated range. Furthermore, the deposition rates of both a-C and a-C:Fe*

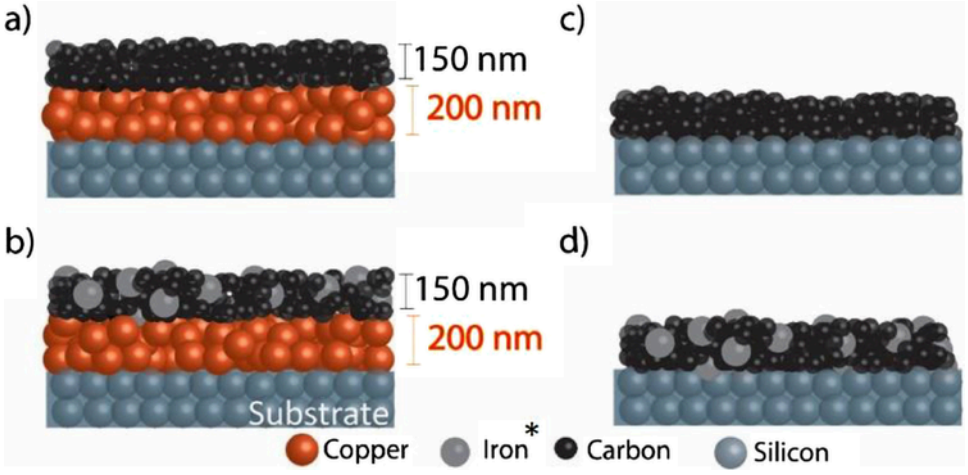

Fig. 1. Schematic representation of the thin film systems investigated in this work. a-b) Double coated samples for reflectance characterization a) The samples referred as a-C/Cu and b) a-C:Fe*/Cu films were deposited onto Cu films previously deposited over Si substrates. c-d) A simpler set of carbon-based films were deposited onto Si substrates for microstructural and electrical characterization, referred as c) a-C/Si and d) a-C:Fe*/Si. All films were grown by DCMS.

Table 1
Average deposition rates at different TSD for a-C and a-C:Fe* films grown using DCMS in Ar at 0.75 Pa and 55 W average power.

TSD [cm]	Deposition rate [nm/min] a-C (carbon target)	Deposition rate [nm/min] a-C:Fe* (mixed target)
2	14.0	25.0
3	8.5	12.7
5	3.1	4.7
10	0.8	1.2

decrease with $1/TSD^2$, as expected for an approximately conical emission of the material from the sputtering target. Note that the deposition rate for a-C:Fe* films is higher (57% on average) compared to pure C deposition, due to the higher deposition rate of iron* compared to carbon [34].

A simpler set (i.e., single layer) of carbon-based films was deposited directly onto Si substrates for microstructural and electrical characterization shown in Fig. 1c-d). In this way, any possible interference of copper could be avoided. All parameters described above for a-C and a-C:Fe* deposition were maintained also for these depositions. These latter systems are hereafter referred to as a-C/Si and a-C:Fe*/Si, respectively. The a-C/Si and a-C:Fe*/Si films were characterized using the following techniques: a Thermo Scientific Verios G4 HP scanning electron microscopy (SEM) operating voltage:1 kV and energy dispersive x-ray spectrometry (EDS) using a ZEISS Sigma HD EDS SAMx using 15 kV. ImageJ software was used for surface analysis of SEM images. Raman spectroscopy using a Witech alpha300 R at 532 nm wavelength magnification 20 X resolution 4 cm^{-1} 9 mW, X-ray diffraction (XRD) using a Bruker goniometer type D8 ADVANCE Plus, operating in the Bragg-Brentano θ−2θ geometry from 20° to 90°, at λ = 0.15418 nm wavelength. The resistivity was measured using the four-point probe method with a Keithley precision current source and a Keithley nanovoltmeter. Film composition and areal density were determined by Rutherford backscattering spectrometry (RBS) using a 1.8 MeV $^4He^+$ beam, and nuclear reaction analysis (NRA) using a 0.950 MeV deuteron beam for C. Mass density was deduced from the areal density and the physical thickness, determined by SEM analysis. Finally optical properties and the total reflection of a-C/Cu and a-C:Fe*/Cu samples (Fig. 1a-b)) were measured using a PerkinElmer lambda35 UV–Vis spectrometer from 400 to 1000 nm (bandwidth of 2 nm) with an 8° sample holder from the monochromatic light beam and a Horiba Jobin Yvon ellipsometer model MM-16, range 430–850 nm for optical constant calculations (*n* and *k*.) using Tauc-Lorentz dispersion model, fitting the acquisition data on Integrated DeltaPsi2 spectroscopic ellipsometry software package.

3. Results and discussions

In general, both films, a-C and a-C:Fe* present a very similar evolution as a function of TSD when referred to as superficial morphology and carbon hybridization. The morphology is discussed for both films deposited at 10 cm from the target since there are some changes in the cluster size as will be presented in the following sections. To avoid repetition, for the other TSD, the smooth surface shown in this section for a-C films is representative of both types films.

In contrast, other properties such as the density and resistivity of a-C and a-C:Fe* films are different and compared.

3.1. Microstructure and composition

All the carbon films deposited in this work were analysed by XRD. The resulting spectra (not presented) show no evidence of crystalline structure. That is, all films are X-ray amorphous with no apparent grain boundaries [25,35]. On the other hand, Raman spectroscopy presents two dispersion bands: the D and G bands typical for sputtered amorphous carbon [25], shown in Fig. 2a-b). The G band indicates the vibrational mode of any sp^2 pair either in aliphatic chains or aromatic rings, and the D band specifies only vibrational modes of sp^2 in aromatic rings (so-called 'breathing modes'). The intensity ratio (I_D/I_G) indicates structural changes in the film, mainly in terms of the film's carbon bonding. The main variation is demonstrated by the arrows in Fig. 2a). I_D/I_G gradually decreases as TSD increases from 2 cm to 10 cm, indicating that the films deposited at 10 cm have a slightly higher content of aliphatic bonds than the films deposited at 2 cm for both a-C and a-C:Fe*. This can be associated with the lower deposition rate and a reduction of the energy of particles participating in the film growth when TSD increases [36]. Comparing films, the main differences are G band position at TSD = 2 cm films shifts from 1547 cm^{-1} to 1566 cm^{-1} the other TSD it sticks around 1547 cm^{-1} for both films. D band shifted from 1355 cm^{-1} to 1371 cm^{-1} a-C to a-C:Fe* respectively [37].

Additionally, I_D/I_G is larger for a-C:Fe* (Fig. 2b)) than for a-C films. According to Ferrari and Robertson [36] (I_D/I_G) is directly proportional to the square of the carbon cluster as in Eq. (1):

$$\frac{I_D}{I_G} = CL_a^{\,2} \tag{1}$$

where C is a constant dependant of the excitation energy used in the Raman analysis and L_a is the graphite cluster size (or in-plane correlation length) [36,37]. The I_D/I_G ratio indicates an increase in the size of sp^2 domains in a-C films as TSD decreases. For a-C:Fe*, the G peak

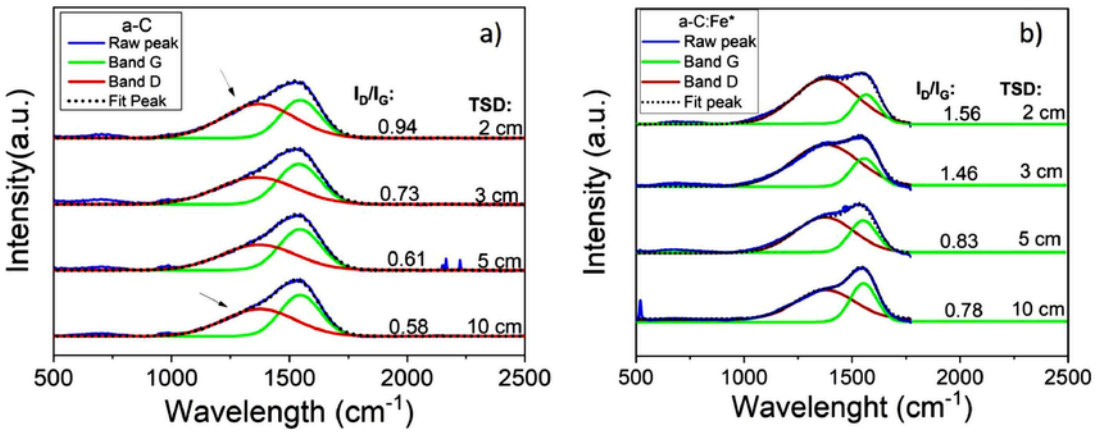

Fig. 2. Raman spectroscopy of 150 nm of a) a-C/Si and b) a-C:Fe*/Si as a function of TSD. I_D/I_G indicates the intensity ration of band D and G.

shifts to higher wave numbers and a wider D peak is consistent with the effect of iron catalysing sp^2 carbon sites [22], and the higher energy of impinging particles for the films deposited closer from the target (smaller TSD) [37].

Topography SEM images of 150 nm carbon thin films deposited on silicon substrates (a-C/Si) at different TSD are presented in Fig. 3a-d).

Generally, the morphology is affected when decreasing TSD a-C films present almost the same compact morphology, however, at TSD = 2 cm, multiple protruding round shapes can be noticed as shown in Fig. 3a). At TSD = 3 and 5 cm, a few of these features can still be noticed, but the surface is generally smooth and continuous (Fig. 3b-c)). At TSD = 10 cm (Fig. 3d)), discernible regular grains are observed. ImageJ analysis gives us an idea of the average size around of 17.5 nm ± 5 nm. These granular structures are typically found in amorphous carbon films.

Previous studies have shown that Fe composite a-C films present granular structures, varying according to the incorporated metal and its quantity [14,20]. The perception of the grains as TSD increases. This grainy surface, sometimes followed by voids between the grains was already observed by Geyer et al. [38] in thin amorphous films.

In Fig. 4 the film's areal density for the a-C/Si samples varies from 1.42 to 1.08 g/cm^3, while for the a-C:Fe*/Si samples it varies from 2.2 to 2.8 g/cm^3 as TSD decreases. The lower density of the films in higher TSD can be attributed to the low deposition energy of precursors, since the substrate was at room temperature [14,25,35]. Indeed, at larger TSD the sputtered species (C and Fe) are more effectively scattered when interacting with the plasma gas (Ar) along their path from the target to the substrate, leading to their thermalization. The mean free path (λ) of the sputtered species depends on the cross-section of elastic neutral-neutral collisions (σ) and the working gas density during deposition (η) [39]. It can be estimated by the following expression:

$$\lambda = \frac{1}{\eta \times \sigma} \tag{2}$$

The probability of having an elastic collision ($P(z)$) can thereby be calculated for any TSD using Eq. (3) [40], where z denotes the TSD, and λ can be estimated using Eq. (3).

$$P(z) = 1 - e^{\left(\frac{-z}{\lambda}\right)} \tag{3}$$

All the $P(z)$ values are given in Table 2, calculated using a typical λ of the C deposition equipment of around 2.7 cm. For a TSD of 10 cm, it is seen that almost all sputtered neutrals will undergo at least one collision with the Ar gas *en route* to the substrate. However, only about half of the sputtered population will collide with the working gas if the substrate is close to the target, TSD = 2 cm (few eV) [41].

From Monte Carlo simulations of sputtered species in DCMS we can get a better estimate of the expected particle velocities depending on TSD. For example, studies on Ti sputtering in Ar show that the peak in the velocity distribution of sputtered Ti changes from about 2000–2600 m/s at 1 cm to close to thermalized at 5 cm (a few hundred m/s) at a working gas pressure of 0.4 Pa [41]. No significant velocity reduction is expected beyond that distance since the particles are already essentially thermalized.

It is well-known that the energy of the film-forming flux is a key factor influencing the microstructure, and affecting adsorption and other elementary processes during thin film growth [40,42,43]. At TSD = 2 cm, energetic particle bombardment increases the mobility of the *adatoms*, resulting in a denser and more homogenous structure of the coating [16]. On the other hand, at 10 cm the high $P(z)$ results in thermalization and a reduced film density in Fig. 3d). It is also worth noting that beyond TSD = 3 cm the density does not change significantly. It is likely associated with the fact that the energy (velocity) of the arriving sputtered species is not reduced much once the particles are closed to being thermalized, which we estimate occurs around 5 cm, as previously discussed. Let us notice, that the scattering on argon is not only slowing down the sputtered species, but it also changes the flight direction reducing the flux of precursors to the substrate, directly linked to the deposition rate. The further the substrate from the target, the larger the amount of sputtered species lost at the (lateral) walls.

NRA and RBS techniques measurements for carbon and iron quantification respectively were carried out after previous EDS. Apart from the Fe detected in the EDS analyses, only traces of Ni were found in the films. The presence of Cr in trace amount cannot be ruled out. This can

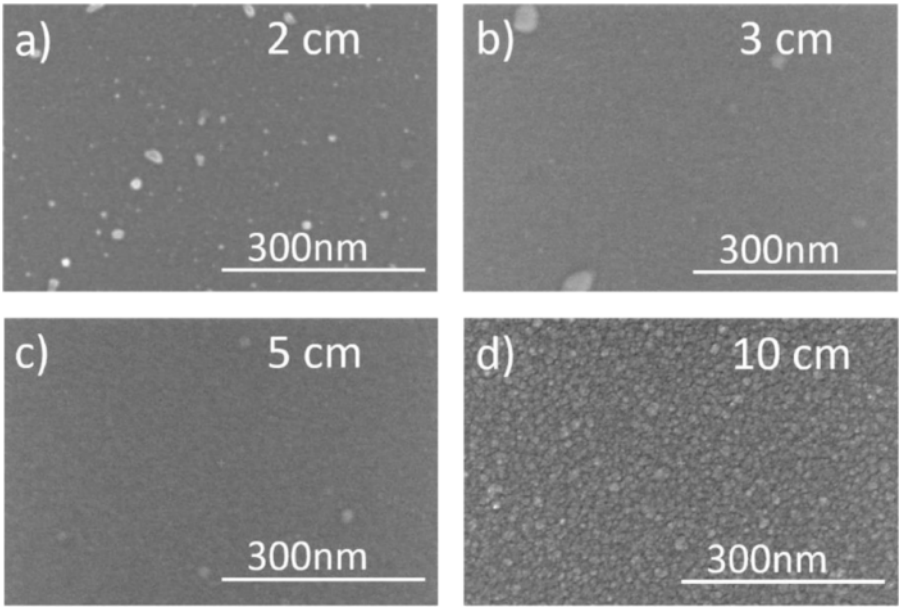

Fig. 3. a-d) Topography SEM images of a-C/Si samples for different TSD.

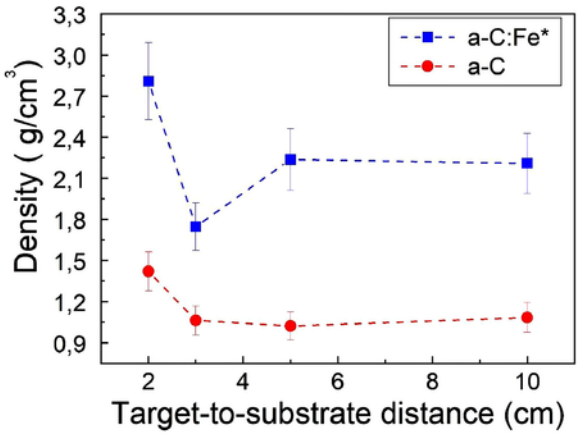

Fig. 4. a-C and a-C:Fe*/Si film areal density as a function of TSD. The dash lines are only to guide the eyes.

Table 2
Estimation of the probabilities for elastic collisions $P(z)$ of sputtered particles for a mean free path of 2.7 cm using 0.75 Pa of Ar for the sputtered thin films.

TSD [cm]	$P(z)$ [%]
2	51
3	66
5	83
10	97

be attributed to the composition of the AISI 316 ring used during deposition (see Section 2) and the sputtering yield of the material. The composition of the a-C:Fe*/Si films were around 50% at. mainly of Fe but traces of Cr and Ni might be considered and 50% at. of carbon for all the analysed samples, and this large compositional difference between the a-C/Si and a-C:Fe*/Si films is also reflected in the film density given in Fig. 4. The RBS spectra showed that the Fe* composition was practically constant within the films [44], with just a small hint of about 10% Fe* depletion in the outer few tens of nm. a-C:Fe*/Si and a-C/Si films present a similar trend for density as a function of TSD. Film areal density is greater for the smallest TSD, and hardly varying for TSD higher than 3 cm, as previously discussed. Consequently, the insertion of 50% at. of iron* is contributing substantially to this high-density value.

3.2. Electrical properties

In the present study the a-C/Si films deposited at TSD = 2 cm and 3 cm have an average resistivity of 2.5×10^5 μΩ cm, see Fig. 5a). This value agrees rather well with sputtered films deposited under similar conditions [45,46]. The resistivity increases dramatically for TSD ≥ 3 cm reaching the limit of our instrument as indicated in Fig. 5a).

On the other hand, the resistivity of the a-C:Fe*/Si films is significantly lower for all studied TSD. At TSD = 2 cm, the resistivity of the a-C:Fe*/Si sample is 1.3×10^3 μΩ cm, i.e., a reduction by two orders of magnitude compared to the corresponding value measured for a-C/Si film. Thus, the addition of Fe* in the carbon matrix, with a bulk resistivity of $\rho_{Fe} = 10.1$ μΩ cm, clearly reduces the global resistivity of the overall structure [27]. This can happen also due to the enhanced iron particles diffusion in the film or due to *threshold percolation* as discussed in the introduction, since no carbides were detected by XRD [47,48]. Solovyev et al. [37] reported very similar resistivities for 50% at Ni amorphous carbon film using magnetron sputtering with negative pulse substrate bias.

The film's resistivity increases sharply as the target-to-substrate distance increases from 2 to 10 cm (Fig. 5a), logarithmic scale). A key factor for the observed resistivity trend as a function of TSD is the film structural changes. Clusters' size plays an important role in the electrical properties of the film. Higher cluster size improves the electron transport in the material and hence reduces the resistivity. The trend in resistivity is thus expected since Raman spectroscopy I_D/I_G implicates in bigger cluster formation resulting in a smoother surface decreasing TSD. Furthermore, the sample deposited at 2 cm is slightly denser/compacted than the one deposited at 10 cm.

In addition, for a-C:Fe*/Si samples, Fig. 5b) shows the topography of an a-C:Fe*/Si sample deposited at 10 cm, comparable to our previous discussion concerning to the a-C/Si samples shown in Fig. 3. A granular surface is again observed and the width of these features is slightly larger (40 nm ± 14 nm) compared to the corresponding a-C thin film (17.5 nm ± 5 nm). Several studies have reported that metal doping generally results in a change in grain size [21,49,50], as well as film density [51], where the latter depends on how the incorporated metal diffuses.

For completeness, the comparably low film resistivity observed for the a-C:Fe*/Si samples can be further optimized by tailoring the film thickness. Fig. 6 demonstrates the dependence of the electrical resistivity at room temperature on a-C:Fe* film thickness deposited at TSD = 2 cm. Basically, the exponential decay of the resistivity, as the film thickness increases. At around a film thickness of 100 nm the resistivity approaches to 1280 μΩ cm, some authors reported neighbouring

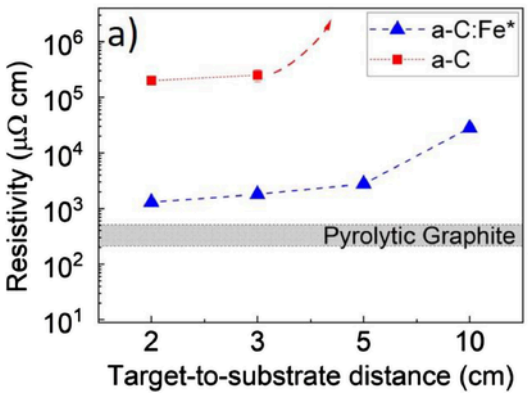

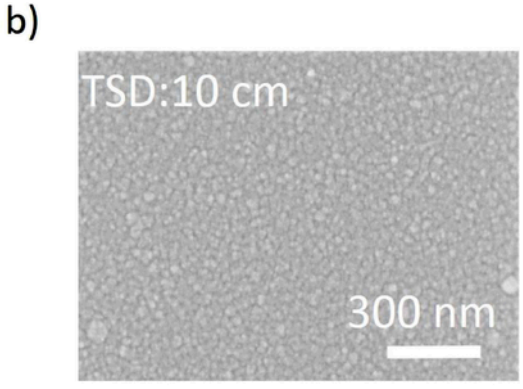

Fig. 5. a) Resistivity measurements of a-C and a-C:Fe* thin films deposited on Si by DCMS at different target-to-substrate distances. Resistivity value for pyrolytic graphite (from [46] is also displayed using logarithmic scale. The dashed lines are only to guide the eye. b) SEM micrograph of the film topography for an a-C:Fe sample deposited at 10 cm.

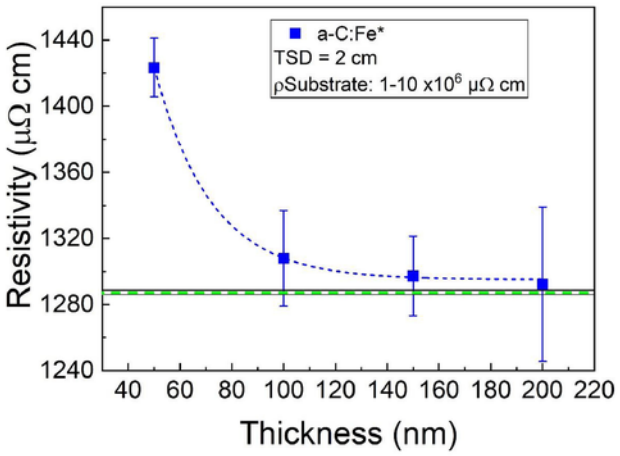

Fig. 6. Film resistivity versus film thickness for a-C:Fe* samples deposited at TSD = 2 cm. The dashed lines are only to guide the eyes.

values for amorphous graphite and others a-C:Me films [19,29,32,37]. The observed trends are in agreement with previously reported theories and experiments concerning cluster size and nucleation related scaling of the resistivity in thin films [52,53].

3.3. Optical properties

Let us now discuss the optical properties of the a-C and a-C:Fe* films deposited onto Cu/Si substrates. Guided by the promising results in terms of morphology, density and resistivity previously presented, we here focus on samples deposited at TSD = 2. A first visual comparison of the pure Cu/Si, a-C/Cu, and a-C:Fe*/Cu sample surfaces can be seen in Fig. 7a-c) along with a schematic representation of the film stack (below each picture). The addition of carbon-based thin films darkens the colour of the entire surface, as expected. The visual aspect does not significantly change between a-C/Cu and a-C:Fe*/Cu.

The total reflectance (TR) in the UV–Vis spectrum of double-coated Si samples of 150 nm a-C/Cu and 150 nm a-C:Fe*/Cu films was measured. Two analyses were carried out in parallel: the first using a UV–Vis spectrophotometer in the range of 400 to 1000 nm, and the second using an optical ellipsometer in the range of 430 nm to 850 nm. Here, results from the spectrophotometer are shown due to its wider spectral range. All results were compared to the same pure Cu/Si reference film.

Fig. 8 summarizes the specular and diffusive reflection (TR) of a-C:Fe*/Cu and a-C/Cu films. One can see that the overall behaviour in reflectance is rather similar for both material systems in the entire broadband spectrum. The Cu/Si reference film exhibits a total reflection of 55% in the blue-green range, from 400 to 550 nm, then it gradually increases to almost 100% in the near-infrared spectrum (around 900 nm). In contrast, the TR of the samples with a-C:Fe* thin films on top of Cu has diminished by almost 70 ± 5% between 400 and 800 nm. Also, the a-C/Cu sample exhibits about 60 ± 5% reduction TR compared to the pure Cu sample at in the same wavelength. A small TR increase of 10% is observed at higher wavelengths (> 800 nm) for both films. In general, similar values were found for both films deposited at TSD = 3 cm (not shown).

The optical properties of the films are attributed to the carbon and film composition [17,25]. The slight decrease in reflectance observed and its lower resistivity confirms that a-C:Fe* is a better light absorber due to the addition of iron*.

In addition, the total reflectance was measured for different film thicknesses for a-C films deposited at TSD = 2 cm. Fig. 9 shows the reflectance versus film thickness. Globally, the total reflectance of the a-C films does not change much in the blue region (400–450 nm) as a function of the thickness (38 ± 5%). The most pronounced TR variation as a function of the film thickness is found beyond 450 nm, in the visible range. In this range a gradual decrease of TR with increasing thickness is seen up to 150 nm, for higher film thickness (≥ 200 nm), TR is constant (30 ± 5%). Furthermore, at higher wavelengths, near IR around 930 nm, TR is about 52% for a-C film up to 150 nm and about 37% for thicker films (≥ 200 nm). The discussions on Fig. 9 continue in Section 3.3.1.

Further in the IR spectrum, around a wavelength of 1000 nm, TR decreases by ≈ 50% for 100 nm a-C film. However, an increased film thickness results in a marginal reduction of the reflectance. Clearly, beyond a thickness of 100 nm, the improvement in the absorption of light is less effective in the near-infrared spectral range.

3.3.1. Ellipsometry measurements

The extinction coefficient, k, and the refraction index, n, of the a-C and a-C:Fe* films were calculated using Tauc-Lorentz dispersion law [15,54,55]. a-C films do not present a clear bandgap but rather a pseudo optical bandgap, where the state density is low but not zero, so a specific model is necessary. Tauc-Lorentz plots used for the calculations are suitable for amorphous semiconductor films [56]. Ellipsometry data was acquired for a-C and a-C:Fe* films deposited on Si at TSD = 2 cm.

The values of n and k found for a-C thin films are in Fig. 10a). They are characteristic of amorphous sputtered carbon [14,46,57]. Generally, a-C films exhibited k values below 1 [58], varying slightly with wavelength indicating that the film is not completely opaque, with par-

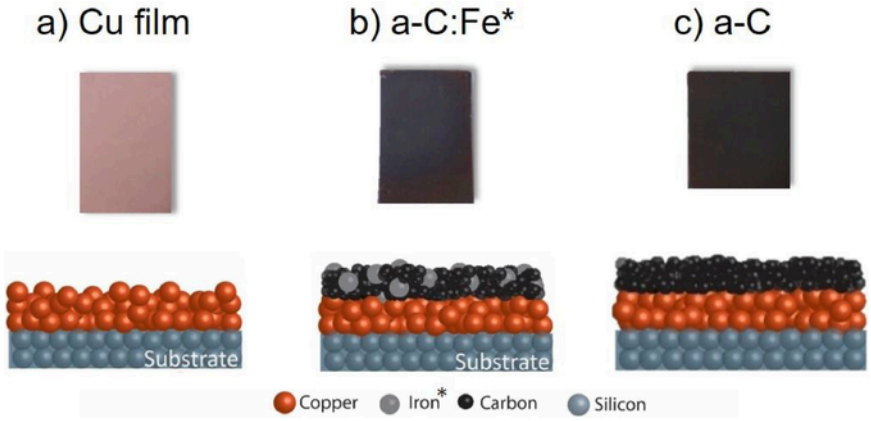

Fig. 7. Top view of the macroscopic surface of double-coated samples. a) Pure Cu film, b) a-C:Fe*/Cu and c) a-C/Cu. The carbon-based film thickness was kept constant at 150 nm deposited at TSD = 2 cm. A schematic representation of the sample cross-section to guide the reader is shown for each film.

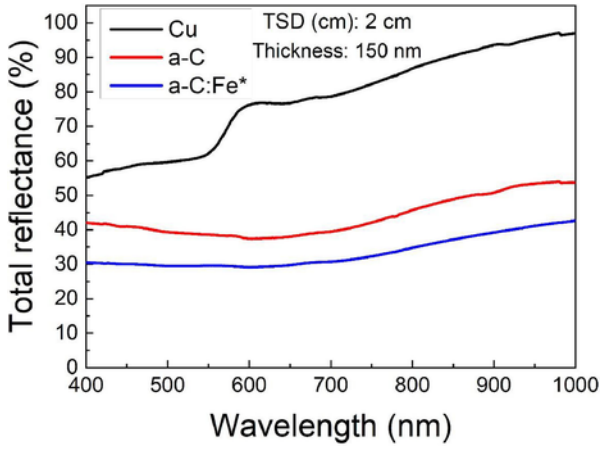

Fig. 8. Total reflectance measured in the UV–Vis spectrum for the different material systems investigated.

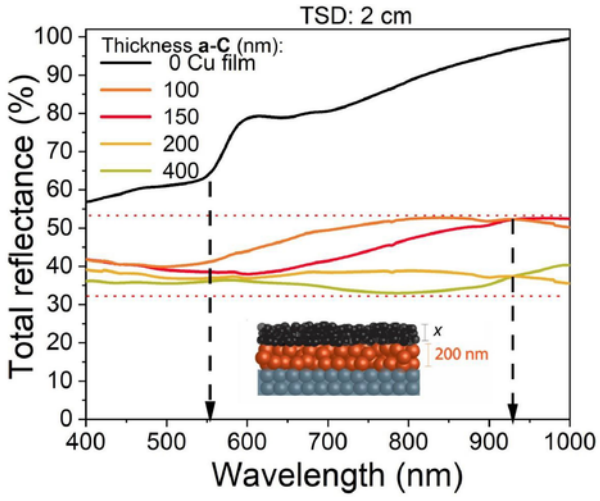

Fig. 9. Total reflectance as a function of a-C thickness deposited at TSD = 2 cm. The inset shows a schematic representation of the transversal section of the sample, the copper film thickness is constant at 200 nm and the a-C film thickness in nm is represented by "*x*".

tial transparency as a function of wavelength. The limited reflection reduction as a function of a-C thin film thickness (Fig. 9) on a copper substrate can thereby be explained by the partial transparency of the film. However, comparing to hydrogenated amorphous carbon films or films deposited by other methods ($k < 0.01$ at 600 nm) [14]), sputtered a-C films have one of the highest absorption coefficients of the amorphous carbon film set [59]. For the a-C:Fe* samples, average k values are above 1.3 reaching a maximum at 1.55 at 850 nm (Fig. 10b)) compared to 0.65 for the a-C sample (Fig. 10a)) in the same wavelength range. It represents an increase of 57% for a-C:Fe*.

Arakawa et al. [11] calculated n and k for glassy carbon films evaporated by arc deposition using Kramers-Kroning analysis. Their results correlate rather well with our results for a-C thin films. Additionally, in Fig. 10 it is seen that n varies from 2 to 2.75 for a-C:Fe* and a-C. Concerning iron, n and k for bulk or thin films are higher than for pure sputtered carbon [60,61], where n reaches values higher than 3 at 850 nm [61]. This could explain the higher values of n and k for a-C:Fe* films and the tendency observed in Fig. 10b) [61,62].

To clarify the influence of the chosen material systems on the total reflectance seen in Fig. 9, we will explore the absorption coefficient, α, and the light penetration depth, D for both material systems investigated. D is the depth that light can penetrate before being absorbed or reflected [55]. Commonly α is estimated to evaluate the light absorption in amorphous semiconductor materials, it is determined by the sum of all electronic transitions [15].

Using Eq. (4), α of the material can be calculated [56]. The inverse of α gives D, i.e., light penetrates more as α decreases. Both parameters are presented in Fig. 11:

$$\alpha = \frac{4\pi k}{\lambda} = \frac{1}{D} \tag{4}$$

The absorption coefficient decreases as a function of increasing wavelength for both films, as displayed in Fig. 11a). Higher values are observed for a-C:Fe* (up to 0.039 in the UV spectrum). For a-C films, α decreases until 700 nm after which it stabilizes around 0.0097.

Concerning the light penetration depth, D, it is seen in Fig. 11b) that the maximum value is approximately 44 nm at 850 nm for the a-C:Fe* film, which is around 59% smaller compared to the a-C film (about 104 nm). The minimum value found for a-C:Fe* is 25 nm compared to 45 nm for a-C films in the UV spectrum. In general, the penetration depth was reduced by at least 40% for the a-C:Fe* film in the entire analysed spectrum (400–850 nm). This great difference can be explained by the differences in the pseudo-optical bandgap found. The addition of iron* decreases the pseudo-optical bandgap by 57% compared to samples without iron*. The pseudo-band gap values are displayed in Fig. 11b) and fit reasonably well with values found in the literature [15,25].

Finally, let us relate the light penetration depth D to the observed total reflectance of a-C versus film thickness seen in Fig. 9. In the shortest wavelength measured, it was found that the light does not penetrate more than 45 nm as shown in Fig. 11b). This agrees well with the

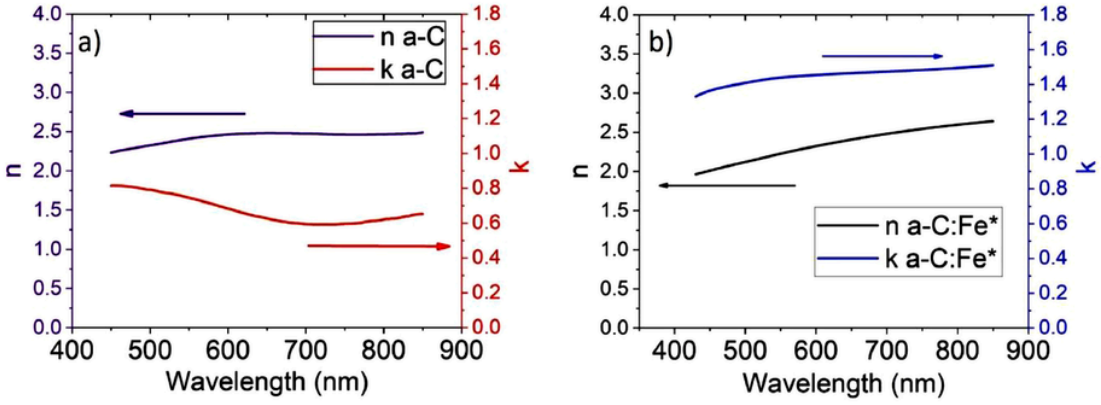

Fig. 10. Refractive index n (left y-axis) and extinction coefficient k (right y-axis) of a 150 nm: a) a-C/Si and b) a-C:Fe*/Si.

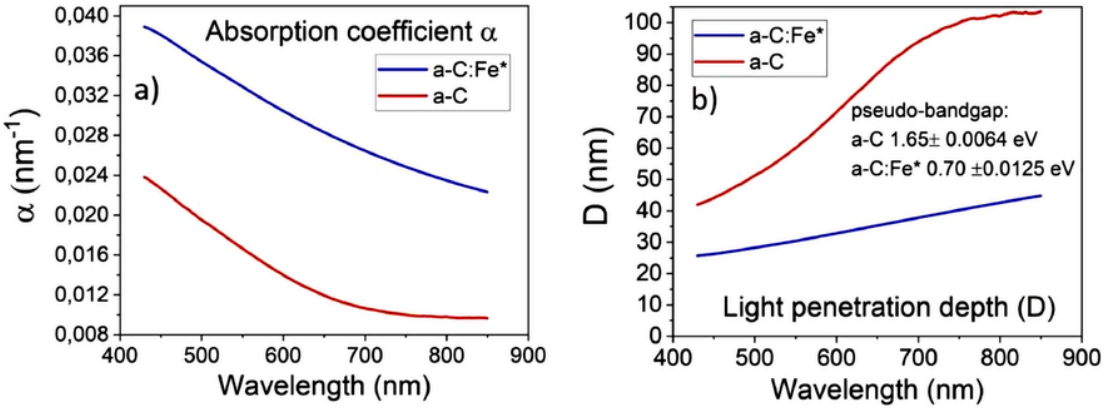

Fig. 11. Estimation of the a) absorption coefficient α and b) penetration depth *D* of light for a-C and a-C:Fe* films deposited at TSD = 2 cm for a film thickness of 150 nm.

observation that the reflectance does not change significantly in the near UV region when the a-C film thickness is greater than the light penetration depth. In the visible range (450–850 nm), the light penetrates deeper, as α and *D* vary, which explains the higher reflectance dependency on the film thickness in this range. From 700 to 850 nm the largest *D*-values are observed, which corroborates well with the largest variation of total reflectance versus film thickness in Fig. 9. For thicknesses much larger than *D*, only negligible variations in the reflectance are observed (around 4% in the visible spectrum between the 200 nm and 400 nm a-C films). This confirms the influence of *D* and α in the total reflectance of the film when deposited over reflective surfaces and explains the variation in the reflectance observed in Fig. 9.

The function of reflectance at normal incidences will be used to clarify the dependence of the reflectance and the parameter *n* and *k* shown in Fig. 10a-b) [63]:

$$R = \frac{(n-1)^2 + k^2}{(n+1)^2 + k^2} \tag{5}$$

Eq. (5) describes the reflectance at one interface for example air/C at normal incidence. Applying this equation to the estimated a-C:Fe* constants we obtain $R = 30 \pm 5\%$ (400–850 nm). It corroborates with the results of total reflectance in Fig. 8 for a-C:Fe* films over reflective surfaces taking into account the low probability for the light reaching the innermost interface (a-C:Fe*/Si) [17,21].

For a-C films, *R* is around 25 ± 10% in the same wavelength range. Now *k* is smaller due to the higher film transparency resulting in a much larger *D*. The innermost interfaces thus play an important role in the reflectance [55,63].

4. Conclusion

Amorphous carbon a-C and a-C:Fe* thin films grown by DCMS can tune the light absorption when deposited on the copper films. a-C:Fe* reduces the total reflectance by up to 70 ± 10%. The incorporation of about 50% at. iron* in the film composition also reduces the resistivity by up to two orders of magnitude compared to a-C films deposited under equivalent conditions. The microstructure of both material systems is modified by varying the target-to-substrate distance, where denser and smoother structures leading to lower film resistivity are obtained close to the target. For a-C:Fe* the absorption coefficient increases if compared to pure a-C films. Light penetration depth explains the total reflectance variation as a function of film thickness for the studied films. These results show that a-C and a-C:Fe* films can be an alternative strategy for anti-reflective coatings on reflective surfaces, such as copper or other reflective metals. Moreover, iron* addition to carbonaceous films shows the possibility of decreasing both resistivity and reflectance.

CRediT authorship contribution statement

Ângela Elisa Crespi: Methodology, Investigation, Data curation, Writing - original draft, Writing - review & editing, Visualization. **Charles Ballage:** Resources, Writing - review & editing. **Marie Christine Hugon:** Methodology, Validation, Data curation, Writing - review & editing, Visualization, Supervision, Project administration. **Jacques Robert:** Data curation, Writing - review & editing, Supervision. **Daniel Lundin:** Data curation, Writing - original draft, Writing - review & editing, Visualization, Supervision, Project administration. **Ian Vickridge:** Validation, Data curation, Writing - review & editing. **José Alvarez:** Validation, Data curation, Writing - review & editing. **Tiberiu Minea:** Methodology, Validation, Writing - review & editing, Visualization, Supervision, Project administration, Funding acquisition.

References

[1] H.K. Raut, V.A. Ganesh, A.S. Nair, S. Ramakrishna, Anti-reflective coatings: a critical, in-depth review, Energy Environ. Sci. 4 (2011) 3779–3804, https://doi.org/10.1039/c1ee01297e.
[2] P. Fan, B. Bai, G. Jin, H. Zhang, M. Zhong, Patternable fabrication of hyper-hierarchical metal surface structures for ultrabroadband antireflection and self-cleaning, Appl. Surf. Sci. 457 (2018) 991–999, https://doi.org/10.1016/j.apsusc.2018.07.017.
[3] A.Y. Vorobyev, C. Guo, Direct femtosecond laser surface nano/microstructuring and its applications, Laser Photonics Rev. 7 (2013) 385–407, https://doi.org/10.1002/lpor.201200017.
[4] A.Y. Vorobyev, A.N. Topkov, O.V. Gurin, V.A. Svich, C. Guo, Enhanced absorption of metals over ultrabroad electromagnetic spectrum, Appl. Phys. Lett. 95 (2009)121106https://doi.org/10.1063/1.3227668.
[5] Y. Yang, J. Yang, C. Liang, H. Wang, Ultra-broadband enhanced absorption of metal surfaces structured by femtosecond laser pulses, Opt. Express. 16 (2008) 11259, https://doi.org/10.1364/OE.16.011259.
[6] J. Huang, C. Liu, Y. Zhu, S. Masala, E. Alarousu, Y. Han, A. Fratalocchi, Harnessing structural darkness in the visible and infrared wavelengths for a new source of

light, Nat. Nanotechnol. 11 (2016) 60–66, https://doi.org/10.1038/nnano.2015.228.
[7] G. Tang, A.C. Hourd, A. Abdolvand, Nanosecond pulsed laser blackening of copper, Appl. Phys. Lett. 101 (2012)231902https://doi.org/10.1063/1.4769215.
[8] D. Shiffler, M. Ruebush, M. Haworth, R. Umstattd, M. LaCour, K. Golby, D. Zagar, T. Knowles, Carbon velvet field-emission cathode, Rev. Sci. Instrum. 73 (2002) 4358–4362, https://doi.org/10.1063/1.1516853.
[9] N.B.É. Sbaï, Couches minces nanostructurées de carbone amorphe dopées ou alliées, Elaboration par ablation laser femtoseconde et Caractérisations, Université Jean Monnet - Saint-Etienne, Français, 2005.
[10] W.W. Duley, Refractive indices for amorphous carbon, Astrophys. J. 287 (1984) 694, https://doi.org/10.1086/162727.
[11] E.T. Arakawa, M.W. Williams, T. Inagaki, Optical properties of arc-evaporated carbon films between 0.6 and 3.8 eV, J. Appl. Phys. 48 (1977) 3176–3177, https://doi.org/10.1063/1.324057.
[12] H. Kovacı, Ö. Baran, A.F. Yetim, Y.B. Bozkurt, L. Kara, A. Çelik, The friction and wear performance of DLC coatings deposited on plasma nitrided AISI 4140 steel by magnetron sputtering under air and vacuum conditions, Surf. Coatings Technol. 349 (2018) 969–979, https://doi.org/10.1016/j.surfcoat.2018.05.084.
[13] Â.E. Crespi, L.M. Leidens, V. Antunes, B.L. Perotti, A.F. Michels, F. Alvarez, C.A. Figueroa, Substrate bias voltage tailoring the interfacial chemistry of a-SiCx:H: a surprising improvement in adhesion of a-C:h thin films deposited on ferrous alloys controlled by oxygen, ACS Appl. Mater. Interfaces. (2019) https://doi.org/10.1021/acsami.9b03597, acsami.9b03597.
[14] J. Vetter, 60 years of DLC coatings: historical highlights and technical review of cathodic arc processes to synthesize various DLC types, and their evolution for industrial applications, Surf. Coatings Technol. 257 (2014) 213–240, https://doi.org/10.1016/j.surfcoat.2014.08.017.
[15] M. Chhowalla, J. Robertson, C.W. Chen, S.R.P. Silva, C.A. Davis, G.A.J. Amaratunga, W.I. Milne, Influence of ion energy and substrate temperature on the optical and electronic properties of tetrahedral amorphous carbon (ta-C) films, J. Appl. Phys. 81 (1997) 139–145, https://doi.org/10.1063/1.364000.
[16] W.G.J.H.M. van Sark, Methods of deposition of hydrogenated amorphous silicon for device applications, in: H.B.T.-H.of T.F. Singh Nalwa (Ed.), Handbook of Thin Film, Elsevier, Burlington, 2002, pp. 1–102, https://doi.org/10.1016/B978-012512908-4/50004-7.
[17] S. Logothetidis, Optical and electronic properties of amorphous carbon materials, Diam. Relat. Mater. 12 (2003) 141–150, https://doi.org/10.1016/S0925-9635(03)00015-3.
[18] K. Bewilogua, D. Hofmann, History of diamond-like carbon films — From first experiments to worldwide applications, Surf. Coatings Technol. 242 (2014) 214–225, https://doi.org/10.1016/j.surfcoat.2014.01.031.
[19] C. Benndorf, E. Boettger, M. Fryda, H.G. Haubold, C.-.P. Klages, H. Köberle, Electrical conductivity and microstructure of metal containing a-C:h films, Synth. Met. 43 (1991) 4055–4058, https://doi.org/10.1016/0379-6779(91)91743-T.
[20] C. Corbella, G. Oncins, M.A. Gómez, M.C. Polo, E. Pascual, J. García-Céspedes, J.L. Andújar, E. Bertran, Structure of diamond-like carbon films containing transition metals deposited by reactive magnetron sputtering, Diam. Relat. Mater. 14 (2005) 1103–1107, https://doi.org/10.1016/j.diamond.2004.10.029.
[21] K.I. Schiffmann, M. Fryda, G. Goerigk, R. Lauer, P. Hinze, A. Bulack, Sizes and distances of metal clusters in Au-, Pt-, W- and Fe-containing diamond-like carbon hard coatings: a comparative study by small angle X-ray scattering, wide angle X-ray diffraction, transmission electron microscopy and scanning tunnelling microsco, Thin Solid Films 347 (1999) 60–71, https://doi.org/10.1016/S0040-6090(98)01607-1.
[22] Y.Y. Wang, S. Gupta, R.J. Nemanich, Role of thin Fe catalyst in the synthesis of double- and single-wall carbon nanotubes via microwave chemical vapor deposition, Appl. Phys. Lett. 85 (2004) 2601–2603, https://doi.org/10.1063/1.1796529.
[23] H.-.Y. Cheng, J.-.W. Chiou, J.-.M. Ting, Y. Tzeng, Reactively co-sputter deposited a-C:h/Cr thin films: material characteristics and optical properties, Thin Solid Films 529 (2013) 164–168, https://doi.org/10.1016/j.tsf.2012.10.025.
[24] H.-.Y. Cheng, W.-.Y. Wu, J.-.M. Ting, Microstructure and optical properties of chromium containing amorphous hydrogenated carbon thin films (a-C:h/Cr), Thin Solid Films 517 (2009) 4724–4727, https://doi.org/10.1016/j.tsf.2009.03.095.
[25] J. Robertson, Diamond-like amorphous carbon, Mater. Sci. Eng. R Rep. 37 (2002) 129–281, https://doi.org/10.1016/S0927-796X(02)00005-0.
[26] S. Neuville, Quantum electronic mechanisms of atomic rearrangements during growth of hard carbon films, Surf. Coatings Technol. 206 (2011) 703–726, https://doi.org/10.1016/j.surfcoat.2011.07.055.
[27] P. Tian, X. Zhang, Q.Z. Xue, Enhanced room-temperature positive magnetoresistance of a-C:fe film, Carbon N. Y. 45 (2007) 1764–1768, https://doi.org/10.1016/j.carbon.2007.05.005.
[28] L.C. Costa, M. Valente, M.A. Sá, F. Henry, Electrical and magnetic properties of Polystyrene doped with Iron nanoparticles, Polym. Bull. 57 (2006) 881–887, https://doi.org/10.1007/s00289-006-0648-6.
[29] S. Craig, G.L. Harding, Composition, optical properties and degradation modes of Cu/(graded metal-carbon) solar selective surfaces, Thin Solid Films 101 (1983) 97–113, https://doi.org/10.1016/0040-6090(83)90262-6.
[30] C.P. Klages, R. Memming, Microstructure and physical properties of metal-containing hydrogenated carbon films, Mater. Sci. Forum. 52–53 (1991) 609–644, https://doi.org/10.4028/www.scientific.net/MSF.52-53.609.
[31] P.K. Mehrotra, R. Hoffmann, Copper(I)-copper(I) interactions. Bonding relationships in d10-d10 systems, Inorg. Chem. 17 (1978) 2187–2189, https://doi.org/10.1021/ic50186a032.
[32] P.I. Vysikaylo, V.S. Mitin, E.E. Son, V.V. Belyaev, Physical Alloying of Plasma Metallization Nanocomposite Coating by Allotropic Carbon Nanostructures—Part 1: experimental Research, IEEE Trans. Plasma Sci. 46 (2018) 1775–1780, https://doi.org/10.1109/TPS.2018.2819138.
[33] F. Cemin, D. Lundin, D. Cammilleri, T. Maroutian, P. Lecoeur, T. Minea, Low electrical resistivity in thin and ultrathin copper layers grown by high power impulse magnetron sputtering, J. Vac. Sci. Technol. A Vacuum, Surfaces, Film. 34 (2016) 51506.
[34] A. Anders, A structure zone diagram including plasma-based deposition and ion etching, Thin Solid Films 518 (2010) 4087–4090, https://doi.org/10.1016/j.tsf.2009.10.145.
[35] J. Robertson, E.P. O'Reilly, Electronic and atomic structure of amorphous carbon, Phys. Rev. B. 35 (1987) 2946–2957, https://doi.org/10.1103/PhysRevB.35.2946.
[36] A.C. Ferrari, J. Robertson, Interpretation of Raman spectra of disordered and amorphous carbon, Phys. Rev. B. 61 (2000) 14095–14107, https://doi.org/10.1103/PhysRevB.61.14095.
[37] A.A. Solovyev, K.V. Oskomov, A.S. Grenadyorov, P.D. Maloney, Preparation of nickel-containing conductive amorphous carbon films by magnetron sputtering with negative high-voltage pulsed substrate bias, Thin Solid Films 650 (2018) 37–43, https://doi.org/10.1016/j.tsf.2018.02.013.
[38] U. Geyer, U. von Hülsen, P. Thiyagarajan, Surface roughening and columnar growth of thin amorphous CuTi films, Appl. Phys. Lett. 70 (1997) 1691–1693, https://doi.org/10.1063/1.118671.
[39] A.V. Phelps, C.H. Greene, J.P. Burke, Collision cross sections for argon atoms with argon atoms for energies from 0.01eV to 10keV, J. Phys. B At. Mol. Opt. Phys. 33 (2000) 2965–2981, https://doi.org/10.1088/0953-4075/33/16/303.
[40] D. Lundin, M. Čada, Z. Hubička, Ionization of sputtered Ti, Al, and C coupled with plasma characterization in HiPIMS, Plasma Sources Sci. Technol. 24 (2015)035018https://doi.org/10.1088/0963-0252/24/3/035018.
[41] D. Lundin, C. Vitelaru, L. de Poucques, N. Brenning, T. Minea, Ti–Ar scattering cross sections by direct comparison of Monte Carlo simulations and laser-induced fluorescence spectroscopy in magnetron discharges, J. Phys. D. Appl. Phys. 46 (2013)175201https://doi.org/10.1088/0022-3727/46/17/175201.
[42] H. Kersten, H. Deutsch, H. Steffen, G.M.W. Kroesen, R. Hippler, The energy balance at substrate surfaces during plasma processing, Vacuum 63 (2001) 385–431, https://doi.org/10.1016/S0042-207X(01)00350-5.
[43] J.A. Thornton, Influence of apparatus geometry and deposition conditions on the structure and topography of thick sputtered coatings, J. Vac. Sci. Technol. 11 (1974) 666–670, https://doi.org/10.1116/1.1312732.
[44] J.-.M. Ting, W.-.Y. Wu, Reactive sputter deposition of metal containing hydrogenated amorphous carbon coatings exhibiting self-assembled alternating nanolayers, Surf. Coatings Technol. 231 (2013) 2–5, https://doi.org/10.1016/j.surfcoat.2012.04.089.
[45] Z. Sun, W. Zhao, D. Kong, Microstructure and Mechanical Property of Magnetron Sputtering Deposited DLC Film, J. Wuhan Univ. Technol. Sci. Ed. 33 (2018) 579–584, https://doi.org/10.1007/s11595-018-1864-2.
[46] H.O. Pierson, Pyrolytic Graphite, in: H.O.B.T.-H.of C. Pierson Graphite, Diamonds and Fullerenes (Eds.), Handbook of Carbon, Graphite, Diamond, And Fullerenes: Properties, Processing, And Applications, Elsevier, Oxford, 1993, pp. 141–165, https://doi.org/10.1016/B978-0-8155-1339-1.50012-8.
[47] Y. Lifshitz, C.D. Roux, K. Boyd, W. Eckstein, J.W. Rabalais, Analysis of carbon film growth from low energy ion beams using dynamic trajectory simulations and Auger electron spectroscopy, Nucl. Instruments Methods Phys. Res. Sect. B Beam Interact. with Mater. Atoms. 83 (1993) 351–356, https://doi.org/10.1016/0168-583X(93)95855-Y.
[48] G. Carter, D.G. Armour, The interaction of low energy ion beams with surfaces, Thin Solid Films 80 (1981) 13–29, https://doi.org/10.1016/0040-6090(81)90202-9.
[49] S. Flege, R. Hatada, A. Hanauer, W. Ensinger, T. Morimura, K. Baba, Preparation of metal-containing diamond-like carbon films by magnetron sputtering and plasma source ion implantation and their properties, Adv. Mater. Sci. Eng. 2017 (2017) 1–8, https://doi.org/10.1155/2017/9082164.
[50] Q. Wei, R.J. Narayan, J. Narayan, J. Sankar, A.K. Sharma, Improvement of wear resistance of pulsed laser deposited diamond-like carbon films through incorporation of metals, Mater. Sci. Eng. B. 53 (1998) 262–266, https://doi.org/10.1016/S0921-5107(98)00150-0.
[51] I. Bouabibsa, S. Lamri, A. Alhussein, T. Minea, F. Sanchette, Plasma investigations and deposition of Me-DLC (Me = Al, Ti or Nb) obtained by a magnetron sputtering-RFPECVD hybrid process, Surf. Coatings Technol. 354 (2018) 351–359, https://doi.org/10.1016/j.surfcoat.2018.09.033.
[52] F. Cemin, D. Lundin, D. Cammilleri, T. Maroutian, P. Lecoeur, T. Minea, Low electrical resistivity in thin and ultrathin copper layers grown by high power impulse magnetron sputtering, J. Vac. Sci. Technol. A Vacuum, Surfaces, Film. 34 (2016)051506https://doi.org/10.1116/1.4959555.
[53] I. Petrov, P.B. Barna, L. Hultman, J.E. Greene, Microstructural evolution during film growth, J. Vac. Sci. Technol. A Vacuum, Surfaces, Film 21 (2003) S117–S128, https://doi.org/10.1116/1.1601610.
[54] D. Gonçalves, E.A. Irene, Fundamentals and applications of spectroscopic ellipsometry, Quim. Nova. 25 (2002) 794–800, https://doi.org/10.1590/S0100-40422002000500015.
[55] R.W. Collins, A.S. Ferlauto, Optical Physics of Materials, Handbook of Ellipsometry, Elsevier, 200593–235, https://doi.org/10.1016/B978-081551499-2.50004-6.

[56] G.E. Jellison, F.A. Modine, Parameterization of the optical functions of amorphous materials in the interband region, Appl. Phys. Lett. 69 (1996) 371–373, https://doi.org/10.1063/1.118064.
[57] S.A. Alterovitz, N. Savvides, F.W. Smith, J.A. Woollam, , Amorphous hydrogenated "diamondlike" carbon films and arc-evaporated carbon films, Handbook of Optical Constants of Solids, Elsevier, 1997837–852, https://doi.org/10.1016/B978-012544415-6.50083-2.
[58] F. Wooten, Interband transitions, Optical Properties of Solids, Elsevier, 1972108–172, https://doi.org/10.1016/B978-0-12-763450-0.50010-6.
[59] A. Erdemir, C. Donnet, Tribology of diamond-like carbon films: recent progress and future prospects, J. Phys. D. Appl. Phys. 39 (2006) R311–R327, https://doi.org/10.1088/0022-3727/39/18/R01.
[60] D.E. Aspnes, The accurate determination of optical properties by ellipsometry, Handbook of Optical Constants of Solids, Elsevier, 199789–112, https://doi.org/10.1016/B978-012544415-6.50008-X.
[61] V.V. Atuchin, V.A. Kochubey, A.S. Kozhukhov, V.N. Kruchinin, L.D. Pokrovsky, I.S. Soldatenkov, I.B. Troitskaia, Microstructure and dispersive optical parameters of iron films deposited by the thermal evaporation method, Optik (Stuttg) 188 (2019) 120–125, https://doi.org/10.1016/j.ijleo.2019.04.122.
[62] W.S.M. Werner, K. Glantschnig, C. Ambrosch-Draxl, Optical constants and inelastic electron-scattering data for 17 elemental metals, J. Phys. Chem. Ref. Data. 38 (2009) 1013–1092, https://doi.org/10.1063/1.3243762.
[63] H. Fujiwara, Reflection and transmission of light, Spectroscopic Ellipsometry Principles and Applications, John Wiley & Sons, 200732–48.